

An adjoint based forecast impact from assimilating MISR winds into the GEOS-5 data assimilation and forecasting system

Kevin J. Mueller¹, Junjie Liu¹, Will McCarty², and Ron Gelaro²

¹ *Jet Propulsion Laboratory, California Institute of Technology;* ² *Goddard Space Flight Center (GSFC)*

Corresponding author: Junjie Liu Junjie.Liu@jpl.nasa.gov

1 Abstract

2 This study examines the benefit of assimilating cloud motion vector (CMV) wind
3 observations obtained from the Multi-angle Imaging SpectroRadiometer (MISR)
4 within a Modern-Era Retrospective Analysis for Research and Applications-2
5 (MERRA2) configuration of the Goddard Earth Observing System-5 (GEOS-5) model
6 Data Assimilation System (DAS). Available in near real time (NRT) and with a
7 record dating back to 1999, MISR CMVs boast pole-to-pole coverage and geometric
8 height assignment that is complementary to the suite of Atmospheric Motion
9 Vectors (AMVs) included in the MERRA2 standard. Experiments spanning
10 September-October-November of 2014 and March-April-May of 2015 estimated
11 relative MISR CMV impact on the 24-hour forecast error reduction with an adjoint
12 based forecast sensitivity method. MISR CMV were more consistently beneficial and
13 provided twice as large a mean forecast benefit when larger uncertainties were
14 assigned to the less accurate component of the CMV oriented along the MISR
15 satellite ground track, as opposed to when equal uncertainties were assigned to the
16 eastward and northward components as in previous studies. Assimilating only the
17 cross-track component provided 60% of the benefit of both components. When
18 optimally assimilated, MISR CMV proved broadly beneficial throughout the Earth,
19 with greatest benefit evident at high latitudes where there is a confluence of more
20 frequent CMV coverage and gaps in coverage from other MERRA2 wind

21 observations. Globally, MISR represented 1.6% of the total forecast benefit, whereas
22 regionally that percentage was as large as 3.7%.

1 **1 Introduction**

2 Atmospheric motion vectors (AMVs), a proxy measure of wind, are
3 indispensable to regional and global numerical weather prediction (NWP) models
4 and analyses. Derived from tracking cloud or water vapor features in satellite
5 imagery, AMVs fill some critical conventional observation data gaps (e.g., the Arctic,
6 Antarctic and global oceans). However, there remain regions where wind
7 observations are sparse or unavailable, notably in the high latitude band (55-65°
8 North/South) between AMVs obtained from regular geosynchronous (GEO)
9 instrument imagery and those obtained from consecutive orbits of lower earth orbit
10 (LEO) instruments. AMVs from composite LEO-GEO (e.g. Lazzara et al., 2014) and
11 from constellations of LEO instruments (e.g. Borde et al., 2016) increasingly, but not
12 entirely, mitigate these gaps. AMVs from LEO are also limited at low levels
13 (pressures > 700 hPa) by concerns about the accuracy of the radiometric heights
14 assigned there, which have led multiple NWP centers to exclude low level AMVs
15 from operational assimilation (Salonen et al., 2015). Cloud motion vector wind
16 observations derived from the Multi-angle Imaging SpectroRadiometer (MISR)
17 instrument onboard the polar-orbiting Terra could help mitigate the above coverage
18 gaps (Mueller et al., 2013), since their heights are retrieved by geometric techniques
19 and their coverage is nearly global and concentrated in the lower troposphere.

20

MISR measures reflected solar radiation in four bands from onboard the sun-synchronous Terra satellite at nine distinct viewing zenith angles including nadir (0°) and four angles (26° , 46° , 60° , and 70°) distributed along-track both forward and aft relative to Terra's flight direction. The motion and height of underlying cloud features are obtained from a single MISR overpass by tracking their progression within 275 m resolution 380 km swath width red band imagery over the 3.5 minute interval between the initial 70° forward view and nadir, and then again for the same interval between nadir and the final 70° aft view (Horvath and Davies, 2001a; Mueller et al., 2013). Aside from the nadir and 70° , a third view angle of 26° is necessarily used to differentiate between parallax and along-track cloud motion. This approach yields a precise geometric height and cross-track wind component, but a relatively less precise along-track wind that is sensitive to the accuracy of feature tracking and georegistration (Zong et al, 2002; Horvath and Davies, 2001). The MISR wind height, cross-track, and along-track components have respective precision of 190 m, 1.1 ms^{-1} , and 1.8 ms^{-1} (Horvath 2013). The retrieval algorithm is attuned to stratocumulus, frequently tracking them despite the presence of overlying clouds with less distinct texture. As a result, the overwhelming majority (>95%) of MISR CMV sampling is found at low levels, and sampling is far better over ocean than land.

The geometric heights assigned to MISR CMVs are not prone to the significant difficulties with radiometric heights assigned to other AMVs, which are recognized as a key limitation to their forecast benefit (Su et al., 2012). AMV height uncertainty accounts for 70% of vector wind differences between other types of AMV and

rawinsonde (Velden et al., 2008). Particularly uncertain are low level radiometric heights (pressures >700 hPa) assigned to broken or semitransparent clouds or in regions where the temperature lapse rate is small (e.g., polar regions) or inverted (e.g., the marine boundary layer). In the arctic, where these conditions are typical, low level AMVs are deemed unreliable (Key et al., 2003; Santek et al., 2010). In comparisons with AMVs derived from the Geostationary Operational Environmental Satellite (GOES), MISR CMVs have been shown to have less biased heights in the 800 hPa – 600 hPa (~2-4 km height) range (Mueller et al., 2017), consistent with similar findings of AMV height bias relative to reanalysis (Salonen et al., 2015). At the same time, MISR CMV heights are prone to uncertainty distinguishing parallax from along-track motion, leading to correlation of error in these components and tendency to overestimate the heights of upper level (> 300 hPa (~7 km)) CMVs, though these comprise less than 5% of total CMV sampling (Mueller et al., 2017).

Several studies have provided preliminary evaluations of the forecast benefit MISR winds might provide. The first of these studies, Baker et al., 2014, employed an adjoint method to quantify the reduction of 24-hour forecast errors from assimilating MISR CMV amongst a suite of additional observations with the NAVy Global Environmental Model (NAVGEM) 4D-Var Data Assimilation System. They found that MISR winds reduced 24-hour global forecast errors, attributing much of that error reduction to lessening a relative dearth of low-level wind observations assimilated by their model. Yamashita (2014) tested assimilation of MISR CMV in addition to routine observations within the 4D-VAR NWP system of the Japan Meteorological Agency, and found increased forecast skill over all. Cress et al., 2014,

assimilated MISR CMV within the operational 3D-VAR numerical weather prediction (NWP) system of the German Weather Service for summer and winter of 2010, finding a benefit to the anomaly correlation of 500 hPa geopotential heights between forecast and analysis.

These previous studies directly assimilated zonal and meridional components of MISR CMV retrievals, with no explicit mechanism to capitalize on the greater accuracy of the cross-track components of winds reported by MISR. In this study, we have decomposed MISR CMV into along-track and cross-track in order to assign appropriate uncertainties to each component and also explored the impact of assimilating only the more accurate cross-track component. Complementing earlier studies, we evaluate the forecast impact of MISR CMV using the Modern-Era Retrospective Analysis for Research and Applications-2 (MERRA2) 3D-VAR configuration of the Goddard Earth Observing System-5 (GEOS-5) model Data Assimilation System (DAS) (Gelaro et al., 2017).

The remaining sections are organized as follows: section 2 describes the datasets, experiments and diagnostic tools used to assess MISR winds benefit to the analysis and forecast. Section 3 summarizes the results, including comparison of techniques and parameters for assimilating MISR winds. Section 4 provides discussion and conclusions.

2 Data and methods

2.1 Review and use of MISR CMV products

Two distinct sources of MISR CMVs are employed in this study, the monthly aggregated MISR Level 3 CMV product and the Level 2 NRT CMV product. The two products are available online and respectively tagged as MI3MCMVN and MI2TC_CMV_HDF_NRT at the NASA Langley Distributed Active Archive Center. The former is available with 24 hour latency archived back to 2000, the latter with NRT latency (95% of CMVS in under 2.5 hours) archived 30 days back from present. Excluded from this study are two other MISR products containing CMV less suitable for assimilation. The MISR Level 2 Cloud product (tagged MIL2TCSP) contains a superset of CMV from the Level 3 CMV product that includes retrievals of lower quality. The MISR Level 2 Stereo product (tagged MIL2TCST) contains less accurate CMV retrieved by a legacy algorithm.

The Level 2 NRT CMV product uses the same retrieval and quality control algorithms as the standard Level 3 CMV product, generating results comparable to the latter. However, the two products have minor differences owing to differences between the NRT and standard processing (STD) versions of upstream Level 0 (L0) and Level 1 (L1) data inputs. The NRT software pipeline is applied to incoming L0 instrument and satellite data in sessions associated with as little as five minutes of data, whereas the standard pipeline operates on the same data consolidated into sessions comprising one full orbit (90 minutes). Without this consolidation, NRT

processing is subject to lost coverage associated with gaps in the availability of necessary inputs at time of processing. Additionally, the continuously updated record of corrections to camera pointing used to perform in-flight geometric calibration is sensitive to the differences between NRT and STD processing. Calibration discrepancies are responsible for a root-mean-square-vector-difference (RMSVD) of 3 m s^{-1} between collocated Level 2 NRT CMVs and Level 3 CMVs (Mueller et al., 2013b).

2.2 GEOS-5 model, assimilation system, and adjoint methodology

This study employs version 5.13.0 of the GEOS-5 DAS, with revisions to support MISR winds assimilation and determination of adjoint sensitivity. Version 5.13.0 is associated with officially released GEOS-5 data products between 20 September 2014 and 1 May 2015. The C180 (1/2 degree latitude-longitude) grid with 72 layers between the surface and 0.01 hPa is employed, with default version 5.13.0 model parameters and assimilated observations (other than MISR CMV) defined by the MERRA-2 reanalysis (Gelaro et al., 2017). MERRA-2 incorporates a broad range of observations, including geostationary AMVs from GOES,

The meteorological analysis in GEOS-5 uses the Gridpoint Statistical Interpolation (GSI) 3D-Var [Wu et al., 2002; Purser et al., 2003a, 2003b] assimilation methods. The objective of the assimilation is to produce an analysis field for which a cost function constructed from the observation-minus-analysis (O-A) residuals is minimized subject to assumed forecast and observation error statistics [Cohn, 1997]. The GSI performs minimization relative to control variables including stream

function contribution from wind, unbalanced velocity potential function, unbalanced temperature, unbalanced surface pressure, moisture, cloud water, ozone, and coefficients for the bias correction of the satellite radiance data.

An adjoint sensitivity method is employed to calculate the impact of each individual observation on the short-range forecast simultaneously, producing results that can be easily aggregated by data type, location, channel, etc [Gelaro et al., 2007; Zhu and Gelaro, 2008; Gelaro et al., 2010]. It is the same method used operationally to monitor and evaluate the impact of assimilated observations. Impacts are measured relative to 24-hour and 30-hour forecast error differences in total moist energy. The forecast error is measured against analysis state at the verification time, $t=24$ hours (Langland and Baker, 2004). The 24-hour and 30-hour forecast are initiated at time, $t=0$ hours, and at time, $t=-6$ hours, respectively. The difference between the former and latter forecasts are due to observations assimilated at the analysis time $t=0$ hours. The method is undertaken for every 6-hour time step, facilitating impact assessment of all assimilated observations in each experiment.

2.3 Experiments

2.3.1 Thinning and screening methods

MISR CMV are reported with 17.6×17.6 gridded resolution with vertical coordinates of height relative to the Earth's ellipsoid. For this study, the set of CMV reported per time step was thinned such that only one CMV could be assimilated per $100 \text{ km} \times 100 \text{ km} \times 100 \text{ hPa}$ volume on a model aligned grid. This thinning included

simple transformation of MISR reported geometric height, h , into pressure coordinates assuming a constant standard atmosphere, that is:

$$p = p_s e^{-kh}$$

where $k=1.186 \times 10^{-4} \text{ m}^{-1}$, and $p_s=1013.25 \text{ hPa}$. Note that this height-pressure conversion formula was only used in the thinning process, while the model geometric height and observation height was used in vertical interpolation during data assimilation process. In addition to spatial thinning, MISR CMV with heights reported below model surface elevation or above 15 km were also excluded. For all the experiments listed in section 2.3.3, a gross-error threshold was also applied to screen CMV differing from background state by more than 8.0 ms^{-1} .

Quality Indicator (QI) values assigned to MISR CMV were given no influence on the uncertainty assigned during assimilation. CMV QI values are a measure of retrieval consistency between neighbors and between redundant forward and aft camera based estimates. German Weather Service experiments found CMV QI to poorly predict CMV influence on forecast skill (Cress, 2014). Consistent with their finding, our own experiments show negligible correlation between per observation MISR CMV forecast impact and QI.

2.3.2 Assimilation methods, uncertainty assignment, and assimilation experiments

Table 1 lists model experiments, three of which differ in the way the winds were assimilated and the uncertainty was assigned to each MISR CMV, all sharing the same September-October-November (SON) time period in 2014. In the first

experiment, labeled UV,, we assimilate MISR zonal (u) and meridional wind (v) directly, the same as the assimilation methods employed in previous MISR wind assimilation studies (e.g., Baker et al., 2014). The uncertainties applied with this method are 3.0 ms^{-1} for the u and v vector components. The components are not treated independently, so either both components are rejected or neither during assimilation. In the second experiment, labeled ATCT, each MISR CMV is translated into along-track and cross-track components based on viewing geometry that are then assimilated independently with respective uncertainties of 8.0 ms^{-1} and 2.0 ms^{-1} . This approach takes advantage of the cross-track having greater theoretical accuracy (Zong et al, 2002; Horvath and Davies, 2001). The assigned uncertainty for the cross-track wind is the same as assessed in validation studies (Horvath 2013, Mueller et al., 2017). The uncertainty of 8.0 m/s for the along-track MISR CMV is conservative, being set much greater than the global along-track RMS difference relative to GOES AMV (3.2 ms^{-1}) in order to limit the potential influence of along-track bias and regions of greater uncertainty (Mueller et al., 2017). In the third experiment, labeled CT, only the more accurate cross-track wind component is assimilated. Lastly, a control experiment, labeled CONTROL, was conducted for the same time period, but with no assimilation of MISR CMV.

In addition to the above experiments comparing assimilation methodology, two variations of the ATCT experiment were conducted using the same assimilation approach. The first, labeled NRT, uses the MISR NRT CMV product rather than the MISR L3 CMV product, to compare their relative effectiveness. The second, labeled ATCT15 extends the timespan of our analysis to March-April-May (MAM) of 2015.

3 Results and Discussion

3.1 Overview

In the following sections, we investigate the performance of three assimilation approaches through comparisons among the CT, UV, and ATCT experiments (3.2); compare the sampling and net impact of MISR CMV relative to other assimilated observations for the ATCT and ATCT_15 experiments (3.3); and assess the consistency of MISR CMV sampling and forecast impact between the NRT CMV and the standard processing (3.4).

3.2 Sensitivity of forecast impact to three methods of assimilating MISR CMVs

Comparisons of mean forecast benefit among ATCT, UV, and CT experiments applying distinct assimilation methodologies to the same data inputs demonstrate the superiority of the ATCT approach. As shown in Table 2, the mean impact per six-hour time step contributed by the assimilated MISR CMV was $-25 \pm 18 \text{ mJ kg}^{-1}$ for ATCT, roughly twice that of UV and 70% greater than that of the CT experiment.

Figures 1d, e, and f present observation-minus-forecast (OMF) (six-hour forecast) statistics, showcasing negligible OMF bias for assimilated cross-track components of MISR CMV during the ATCT experiment, but bias as large as 2.0 m s^{-1} for the along-track component. In the absence of model or observation bias, OMF should be unbiased (e.g., Kalnay 2003). Here, along-track OMF bias follows a pattern broadly consistent with that seen in comparison between MISR CMVs and GOES AMVs (Mueller et al., 2017). The along-track component bias at lower levels (below 750 hPa) is proportional to height. The bias changes from negative to

220 positive around the peak height of sampling density, at 850 hPa in the top row of
221 Figure 1. This is a consequence of the correlation (Zong et al., 2002) between error
222 in the height and error in the along-track component of MISR CMVs causing
223 preferential sampling of negative/positive along-track bias at heights below/above
224 the peak in sampling. Above 750 hPa, MISR CMV along-track bias has no such
225 gradient, instead being consistently on the order of $1\text{-}2\text{ ms}^{-1}$ at high latitudes where
226 the majority of sampling is found. Over the tropics, where sampling is sparse, the
227 bias is not evident. Figures 1d, 1e, and 1f also show bias profiles for the UV
228 experiment, wherein the same underlying positive along-track bias manifests as
229 principally southward component bias at low latitudes and both westward and
230 southward bias at mid to high latitudes.

231 Evident in Figures 1g, h, and j, heights and regions where the along-track bias is
232 most pronounced in the ATCT experiment also show the largest discrepancies
233 between UV and ATCT in the forecast error reduction. This is most evident in the
234 southern extra-tropics where assimilation of the v component in the UV experiment
235 actually degrades the forecast for mid-level CMVs at heights from 900 hPa to 500
236 hPa. In contrast, the along-track component in the ATCT experiment is consistently
237 beneficial. In contrast to the v component, the assimilated u component consistently
238 improves the forecast, but to a far lesser degree than the assimilated cross-track
239 component in the ATCT experiment, which is largely due to the large u component
240 bias (Figure 1d, e, and f) and random errors relative to cross-track component (2.5
241 m/s vs. 2.1 m/s). It is also evident in Figures 1a, 1b, and 1c that the same heights
242 and regions where the v -component degraded the UV forecast also produced a

243 greater number of rejected CMV in UV relative to ATCT. The northern extra-tropics
244 exhibit the same trends as above, though to a lesser extent. The trends observed in
245 the tropics represent an instructive counterpoint. Because the mean along-track
246 bias is less consistent and not as large there, and because the projection of cross-
247 track and along-track winds is more aligned with u and v components there, the
248 forecast benefit is roughly equivalent for the ATCT and UV experiments.

249 For the CT experiment, the along-track component was excluded all together.
250 As evident for all latitude bands (Figures 1g, h, and i), assimilating CT only
251 consistently reduced the forecast error, but choosing not to assimilate the along-
252 track component had an adverse effect on the benefit provided by the cross-track
253 component, especially over the extra-tropics, reducing its benefit by as much as
254 40%. Riishojgard et al. (2008) also showed that single wind component
255 assimilation produced a poorer representation of that field in the analysis state.
256 They argued that the analysis accuracy of single wind assimilation depends more on
257 the forecast error covariance specified in data assimilation compared to assimilating
258 two wind components. Stoffelen et al. (2005) and Marseille et al. (2008) also argued
259 that proper background error covariance is essential to maximize single wind
260 observation impact. In CT, we used the same forecast error covariance as in the
261 ATCT case. The poorer performance of CT indicates that the default forecast error
262 covariance does not accurately capture the relationships between different
263 dynamical variables. Since the wind and mass fields, such as pressure, are more
264 tightly coupled over the extra-tropics in the forecast error covariance, the

degradation of assimilating a single component is larger over the extra-tropics compared to the tropics (Figure 1g, h, and i).

3.3 MISR forecast impact relative to other instruments

The global 24-hour forecast impact amongst MISR CMVs and other classes of satellite instruments is compared for the ATCT_15 experiment in Figure 2a. (The results of the comparable ATCT experiment are roughly equivalent, with minor differences discussed in section 3.4). MISR CMVs represent 1.6% of the total forecast benefit from all of the observations, while AMVs from lower earth orbit (LEO) and geosynchronous (GEO) represent ~15%. The total impact of satellite winds is second behind that of infrared (IR) and microwave (MW) radiance observations, which represent just over 50%. Rawinsonde and dropsonde profiles (labeled RAOB+SND) and in-situ aircraft measurements that include wind, temperature, and pressure each represent another ~12%. Surface wind forcing as measured by microwave scatterometers represent 1% of impact. An additional 10% of forecast impact not plotted in Figure 2a is contributed by various land- and ship-based observations, by radio occultation observations, and by pilot-balloon measurements of wind. Figure 2b shows the per-obs impact of MISR CMV to be the largest of the above observation groups, with magnitude comparable to RAOB+SND.

MISR CMVs are broadly beneficial everywhere, with greatest benefit evident at high latitudes where there is a confluence of more frequent CMV coverage and gaps in coverage from other wind observations. For example, Figure 2c shows that MISR CMV contributes 3.7% of the total forecast benefit between latitudes 55° and 70° South, more than double that of the global mean forecast impact of 1.6%. Figure 3

shows coverage for classes of wind observations, where coverage is defined by the fraction of 6 hour periods during which one or more observation was assimilated within each 2.5° latitude \times 2.5° longitude grid cell. Figure 3a shows the frequency of CMV coverage in the months of SON to be under 10% at low latitudes, and up to 20% or 50% depending on season at high latitudes. MISR CMV coverage is primarily governed by the satellite repeat interval, varying from 9 days at the equator to as little as 90 minutes near the poles, and by seasonal variation of available sunlight at high latitudes. Greater MISR CMV sampling at high latitudes synergistically coincides with gaps between LEO and GEO AMV coverage evident in Figure 3b, ultimately producing greater forecast benefit for those regions as evident in Figure 4a. Over the Southern Ocean, these regions also coincide with a paucity of aircraft and sonde observations (Figures 3d & 3e), and, correspondingly, even greater forecast benefit. Another region of enhanced MISR CMV benefit (Figure 4a) is found over central Asia in the gap between GEO AMVs captured from Meteosat-9 and MTSAT-2 instruments (Figure 3b). The region also lacks frequent coverage from aircraft and sondes (Figures 3e & 3f), to the extent that the rare instances of MISR CMV retrieved there have outsized influence. Over ocean, the geographic distribution of forecast benefit from MISR CMVs is rather similar to that of scatterometer winds, possibly reflecting the fact that both largely or entirely provide low level constraints on the wind field (Figures 3c and 4c). For example, both provide negligible benefit over large swaths of the tropical Pacific and Atlantic oceans, which is primarily due to the dense wind observations from the default LEO and GEO satellites (Figure 4b). Although the forecast benefit from MISR CMV is

evidently enhanced where coverage from other wind observations is sparse, MISR CMVs also exhibit significant benefits in well-sampled regions such as the North Pacific.

3.4 Sensitivity of MISR wind forecast impact to assimilation time period and MISR CMV products

ATCT₁₅ and ATCT were carried out over two different seasons: boreal summer and fall respectively. Comparing these two experiments helps identify the sensitivity of MISR wind impact to time of year, while aggregating them provides six months of simulation. On a daily basis, MISR CMVs provide a consistent 24-hour forecast benefit throughout ATCT and ATCT₁₅ as indicated in Figure 5 by a time series of per orbit forecast impact wherein the running mean over 15 orbits (i.e. the rough equivalent of 24 hours) is always beneficial (i.e. negative contribution to forecast error norm). Measurements of forecast impact are inherently noisy, with the standard deviation of per orbit CMV impact having comparable magnitude to the mean, that is $10 \text{ J kg}^{-1} \times 10^{-3}$. Still, the overwhelming majority (88%) of orbits with MISR CMV sampling are found to provide a net forecast benefit, while the infrequent remainder is broadly distributed, such that no duration of sequential orbits contributes a significant regression. The largest single orbit forecast regression is $28.9 \text{ J kg}^{-1} \times 10^{-3}$ during ATCT. As visualized in Figure 5 and Table 2, the number of MISR CMV assimilated on a per-orbit basis (2500) varies little (± 360) in ATCT or ATCT₁₅. Nor does the number of CMV rejected (330 ± 110) during computation of model analysis state through incremental minimization of the GSI cost function.

The near equivalence of CMV six-hourly forecast impacts in ATCT and ATCT_15 is a coincidental byproduct of ATCT producing 16% greater impact per orbit offset by 25% fewer orbits producing valid CMV sampling. The greater per-orbit CMV benefit in ATCT can be traced to seasonality of sampling, with ATCT having a greater fraction of total sampling located over the Southern Ocean where the model most benefits from assimilating CMVs. The sampling deficit in ATCT can be traced to two gaps evident in Figure 5 that were caused by a temporary suboptimal software configuration affecting Terra attitude data that had been used in the MISR standard processing chain during September 2014. The underlying issue, which was identified and rectified in November 2014, did not affect other Terra instruments or MISR science products, and also did not affect MISR NRT processing- hence the absence of gaps in Figure 6 corresponding to those evident in Figure 5.

Figure 6 shows time series of the MISR CMVs impact and observation count in the NRT experiment, which assimilates MISR NRT CMVs. Relative to standard processing, the NRT CMVs are prone to losses of sampling due to timeliness of necessary data input. As a result, NRT assimilates less samples per orbit (1900) with greater variability of per orbit sampling (± 600). Relative to ATCT, the fraction of sampling in NRT (76%) is consistent with the fraction of forecast benefit (72%)- that is 6.8 out of 9.5 $\text{J kg}^{-1} \times 10^{-3}$. The distribution and magnitude of forecast regressions on a per orbit basis are also comparable to ATCT.

4 Conclusions

A series of experiments have been conducted, demonstrating the benefit of assimilating cloud motion vectors from the MISR CMVs over periods covering September-October-November of 2014 and March-April-May within the GEOS-5 DAS as determined by an adjoint based forecast sensitivity method. Whereas previous studies have directly assimilated the zonal and meridional components of MISR CMVs, this study demonstrates more consistently beneficial and twice as large a mean forecast benefit when assimilating along-track and cross-track components and assigning larger uncertainties to less accurate along-track component. Although the more certain cross-track component contributes more than 90% of the total forecast benefit when assimilating both along-track and cross-track, assimilating only the latter provides only 60% of the forecast benefit as both. Systematic along-track bias in MISR CMVs consistent with earlier studies was evident in OMF statistics. This factored into the benefits of assigning greater uncertainty to the along-track. Another approach worth investigating would be application of a height- and possibly latitude- dependent along-track bias correction.

The overall benefit of optimally assimilating MISR CMVs was a 1.6% contribution to the global reduction of the moist energy error norm for 24-hour forecasts, with about twice that percentage of contribution in regions such as the Southern Ocean that are less well observed. Note that the impact on 24-hour forecast error reduction is only one measure of the observation impact. The overall reduction on 24-hour forecast errors from assimilating MISR winds corroborates

earlier studies showing an overall benefit from MISR CMVs as measured by various metrics within multiple models (e.g., Yamashita (2014)). The magnitude of benefit is promising in regard to the multi-angle retrieval of CMVs, given the limitations on MISR coverage imposed by its relatively narrow 360 km swath. A single wider-swath multi-angle imager, a tandem convoy of such imagers (which avoids the ambiguity between parallax and along-track motion), or a multitude of low cost nano-satellite variants could all provide significantly greater forecast benefit.

5 ACKNOWLEDGMENTS

We acknowledge the funding support from NASA data for operational analysis (NDOA) program under grant NNH13ZDA001N . We acknowledge the technical support from Joe Stassi (GMAO), Dan Holdaway (GMAO), and Meta Sienkiewicz (GMAO). We appreciate the instructive comments and discussions with Dr. Nancy Baker (NRL), and the support from Dr. Dave Diner (JPL), Veljko Jovanovic (JPL), and Michael Garay (JPL). All the calculations were carried out with the supercomputer from NASA center for climate simulations (NCCS). This research was carried out at Jet Propulsion Laboratory, California Institute of Technology, under contract with the National Aeronautics and Space Administration.

6 REFERENCES

- Baker, N. L., P. M. Pauley, R. H. Langland, K. Mueller, and D. Wu, 2014: An assessment of the impact of the assimilation of NASA TERRA MISR atmospheric motion vectors on the NRL global atmospheric prediction system. *Second Symposium on the Joint Center for Satellite Data Assimilation, 94th American Meteorological Society Annual Meeting. Atlanta, Georgia, Georgia World Congress Center.*
http://www.jcsda.noaa.gov/documents/meetings/AMS2014/2nd_JCSDA_Baker_MISR.pptx
- Borde, R., O. Hautecoeur, and M. Carranza. (2016) EUMETSAT Global AVHRR Wind Product. *J. Atmos. Ocean. Tech.*, **133**, 429-438
- Cohn, S. E., 1997: An introduction to estimation theory. *J. Meteor. Soc. Japan*, 75, 257-288
- Cress, A., (2014) Improving the Use of Satellite Winds at the German Weather Service, (2014) *Twelfth International Winds Workshop*, Copenhagen, Denmark.
http://www.eumetsat.int/website/wcm/idc/idcplg?IdcService=GET_FILE&dDocName=PDF_CONF_P61_S4_02_CRESS_V&RevisionSelectionMethod=LatestReleased&Rendition=Web
- Gelaro, R., Y. Zhu, and R. M. Errico, 2007: Examination of various-order adjoint-based approximations of observation impact. *Meteorologische Zeitschrift* **16**, 685–692.
- Gelaro R., R. H. Langland, S., Pellerin, and R. Todling, 2010: The THORPEX observation impact inter-comparison experiment. *Mon. Weather Rev.* **138**: 4009–4025.

23 Gelaro, R., and Coauthors, 2017: The Modern-Era Retrospective Analysis for Research
 24 and Applications, version 2 (MERRA-2). *J. Climate*, **30**, 5419–5454
 25 Horvath, Á. and R. Davies, 2001: Feasibility and error analysis of cloud motion wind
 26 extraction from near-simultaneous multiangle MISR measurements, *Journal of*
 27 *Atmospheric and Oceanic Technology*, 18-4, 591-608
 28 Horváth, Á. 2013: Improvements to MISR stereo motion vectors., *J. Geophys. Res.*, 118
 29 Kalnay, E. (2003), *Atmospheric Modeling, Data Assimilation, and Predictability*, 341
 30 pp., Cambridge Univ. Press, New York
 31 Key, J. R., D. Santek, C. S. Velden, N. Bormann, J.-N. Thépaut, L. P. Riishøjgaard, Y.
 32 Zhu, and W. P. Menzel, 2003: Cloud-drift and water vapor winds in the polar regions
 33 from MODIS. *IEEE Trans. Geosci. Remote Sens.*, **41**, 482–492.
 34 Langland, R. H., and N. Baker, 2004: Estimation of observation impact using the NRL
 35 atmospheric variational data assimilation adjoint system. *Tellus*, 56, 189–201.
 36 Lazzara, M.A., R. ATCTorak, D.A. Santek, B.T. Hoover, C.S. Velden, and J.R. Key,
 37 2014. High-Latitude Atmospheric Motion Vectors from Composite Satellite Data. *J.*
 38 *Appl. Meteor. Clim.* 53, 534-547.
 39 Marseille, G. J., A. Stoffelen, J. Barkmeijer, 2008. Sensitivity Observing System
 40 Experiment (SOSE) - A New Effective NWP-based Tool in Designing the Global
 41 Observing System. *Tellus*, A, 1, 60, 216-233, 10.1111/j.1600-0870.2007.00288.x
 42 Mueller, K.J., M.J. Garay, C. Moroney, and V. Jovanovic, 2012: “Enhanced MISR Cloud
 43 Motion Vectors: Performance Evaluation Relative to RAOB, MODIS, and GOES,”
 44 11th International Winds Workshop, Auckland, New Zealand

45 Mueller, K.J., C.M. Moroney, V. Jovanovic, M.J. Garay, J-P Muller, L. Di Girolamo, and
 46 R. Davies, 2013a: MISR Level 2 Cloud Product Algorithm Theoretical Basis, JPL D-
 47 73327
 48 http://eospso.gsfc.nasa.gov/sites/default/files/atbd/MISR_L2_CLOUD_ATBD-1.pdf
 49 Mueller, K.J., C.M. Moroney, and V. Jovanovic, 2013b: "MISR Level 2 Cloud Product
 50 Quality Statement, September 14, 2012",
 51 https://eosweb.larc.nasa.gov/sites/default/files/project/misr/quality_summaries/L2TC
 52 [_Cloud_Product.pdf](https://eosweb.larc.nasa.gov/sites/default/files/project/misr/quality_summaries/L2TC_Cloud_Product.pdf)
 53 Mueller, K.J., D.L. Wu, A. Horvath, V.M. Jovanovic, J.-P. Muller, L.D. DiGirolamo, M.J.
 54 . Garay, D.J. Diner, C.M. Moroney, and S.Wanzong, 2017: Assessment of MISR Clo
 55 ud Motion Vectors (CMVs) relative to GOES and MODIS Atmospheric Motion Vect
 56 ors (AMVs). *J. Appl. Meteor. Climat.* doi:10.1175/JAMC-D-16-0112.1, in press.
 57 Purser, R. J., W. Wu, D. F. Parrish, and N. M. Roberts, 2003a: Numerical aspects of the
 58 application of recursive filters to variational statistical analysis. Part I: Spatially
 59 homogeneous and isotropic Gaussian covariances. *Mon. Wea. Rev.*, **131**, 1524–1535.
 60 Purser, R.J., W.-S. Wu, D.F. Parrish, and N.M. Roberts, 2003b: Numerical aspects of the
 61 application of recursive filters to variational statistical analysis. Part II: Spatially
 62 inhomogeneous and anisotropic general covariances. *Mon. Wea. Rev.*, **131**, pp. 1536-
 63 1548.
 64 Riishøjgaard, L.P., R. Atlas, and G. D. Emmitt, 2008: The Impact of ATCTL
 65 Observations on a Single-Level Meteorological Analysis. *J. Appl. Meteorol.* **44**,
 66 1276–1277

67 Salonen, K., J. Cotton, N. Bormann, and M. Forsythe, 2015: Characterizing AMV
68 Height-Assignment Error by Comparing Best-Fit Pressure Statistics from the
69 Met Office and ECMWF Data Assimilation Systems. *J. Appl Climatol.*, 54, 225-242

70 Santek, D. 2010: The Impact of Satellite-Derived Polar Winds on Lower-Latitude
71 Forecasts. *Mon. Wea. Rev.*, **138**, 123–139

72 Stoffelen, A., G.J. Marseille, E. Andersson and D.G.H. Tan, 2005: Comments on The
73 Impact of Doppler Wind Observations on a Single-Level Meteorological Analysis
74 by L.P. Riishojgaard, R. Atlas and G.D. Emmitt, *J. Appl. Meteor.*, 44, 1276-1277.

75 Su, X., J. Derber, and J. Jung, 2012: Recent work on Satellite atmospheric motion
76 vectors in the NCEP data assimilation system. 11th International winds
77 workshop. February 20-24, 2012, Auckland, New Zealand

78 Wu, W.-S., R.J. Purser and D.F. Parrish, 2002: Three-dimensional variational analysis
79 with spatially inhomogeneous covariances. *Mon. Wea. Rev.*, **130**, 2905-2916.

80 Yamashita, K, (2014) The Impact of NASA TERRA MISR Atmospheric Motion Vector
81 Assimilation into JMA's Operational Global NWP System. *CAS/JSC WGNE Res.*
82 *Activ. Atmos. Oceanic Model*: [http://www.wcrp-](http://www.wcrp-climate.org/WGNE/BlueBook/2014/individual-articles/01_Yamashita_Koji_WGNE_BB2014_MISR_yamashita_final.pdf)
83 [climate.org/WGNE/BlueBook/2014/individual-](http://www.wcrp-climate.org/WGNE/BlueBook/2014/individual-articles/01_Yamashita_Koji_WGNE_BB2014_MISR_yamashita_final.pdf)
84 [articles/01_Yamashita_Koji_WGNE_BB2014_MISR_yamashita_final.pdf](http://www.wcrp-climate.org/WGNE/BlueBook/2014/individual-articles/01_Yamashita_Koji_WGNE_BB2014_MISR_yamashita_final.pdf)

85 Zhu, Y., L. P. Riishojgaard, R. Davies, and C. Moroney, 2004: "Assessment and
86 application of MISR winds". 7th Int. Winds Workshop, Helsinki, Finland.

87 Zhu, Y. and R. Gelaro, 2008: Observation Sensitivity Calculations Using the Adjoint of
88 the Gridpoint Statistical Interpolation (GSI) Analysis System. *Mon. Wea. Rev.*,

89 **136**, 335–351. doi: <http://dx.doi.org/10.1175/MWR3525.1>

90

Figure Captions

Figure 1: Vertical profiles of per component forecast impact of UV, ATCT, and CT experiments

Vertical profiles for the southern hemisphere extra-tropics (left; a,d,g), the tropics (middle; b,e,h), and the northern hemisphere extra-tropics (right; c,f,i), are shown for sampling (top; a,b,c), observation minus 6-hour forecast (middle; d,e,f), and forecast impact (bottom; g,h,i) for the u and v components of MISR CMV in the UV experiment (labeled $uv\ u$ and $uv\ v$ in legend); the along-track ($ATCT\ at$) and cross-track ($ATCT\ ct$) in ATCT; and the cross-track components ($ct\ ct$) in CT.

Figure 2: Forecast impact of various observation types in ATCT and ATCT_15 experiments

The mean 24-hour forecast global (top; a,b) and a select regional (bottom; c,d) impact for selected types of observations in the ATCT_15 experiments as accumulated per 6-hours (left; a,c) and per observation (right; b,d). Error bars representing standard deviations are given, alongside percentages of total impact.

Figure 3: Mapped coverage of MISR CMVs relative to other classes of observation

Mapped coverage for five classes of observations assimilated in ATCT and ATCT_15 experiments spanning Sep.-Nov. 2014 and Mar.-May 2015. Coverage is measured per 2.5° latitude \times 2.5° longitude map grid cell by the fraction of six-hour periods throughout experiments during which one or more observations were assimilated within that grid cell.

Figure 4: Adjoint forecast impact of MISR CMVs relative to other classes of observation.

As in Figure 2, but showing mean forecast impact accumulated per six-hour period in each map grid cell.

Figure 5: Time series of MISR CMV sampling and forecast impact per orbit for ATCT and ATCT_15

Time series of forecast impacts (top; a,b) and observation counts (bottom; c,d) for MISR CMV data during ATCT experiment (left; a,c) from Sep.-Nov. 2014 and ATCT_15 experiment (right; b,d) from Mar.-May 2015. Orbits with a net negative (i.e. beneficial) forecast impact are indicated in blue, the rest in red. Minima and maxima are shown in upper right. A running mean over 15 orbits (i.e. ~ 1 day) is plotted in black. Numbers of observations per orbit that were assimilated (blue) and rejected (red) are shown alongside a 15 orbit running mean (black).

Figure 6: Time series of MISR CMV sampling and forecast impact per orbit for NRT

As in Figure 5, but for experiment NRT.

134
135
136

137

138 **7 Tables**139 **Table 1 List of experiments, durations, and assimilation methods**

Experiment	Duration of experiment	MISR data product	Method of assimilating MISR winds
CONTROL	2014/09/02 - 2014/12/01	none	none
UV	2014/09/02 - 2014/12/01	MISR L3 CMV	joint u and v components
ATCT	2014/09/02 - 2014/12/01	MISR L3 CMV	independent along-track and cross-track components
CT	2014/09/02 - 2014/12/01	MISR L3 CMV	Only cross-track component
ATCT_15	2015/03/01 - 2015/06/01	MISR L3 CMV	independent along-track and cross-track components
ATCT_NRT	2014/09/02 - 2014/12/01	MISR NRT CMV	independent along-track and cross-track components

140

141 **Table 2 Overview of experiment statistics**

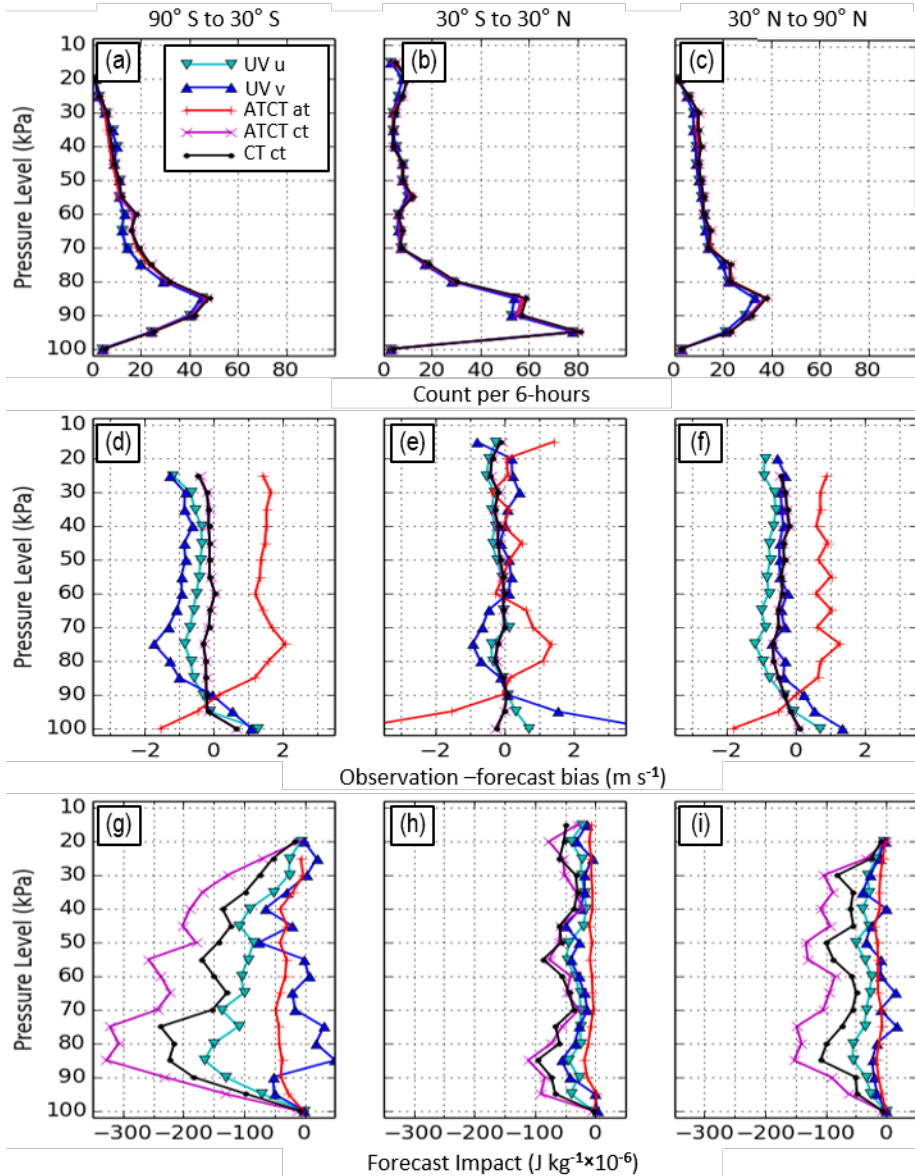
Label	MISR obs. per 6-hours	MISR obs. per valid orbit	MISR reject obs. per valid orbit	MISR impact per 6-hours ($\text{J kg}^{-1} \times 10^{-3}$)	MISR impact per valid orbit ($\text{J kg}^{-1} \times 10^{-3}$)	MISR impact per obs. ($\text{J kg}^{-1} \times 10^{-6}$)
UV	6000±3000	2400±360	520±160	-12±18	-4.8±10.4	-2.0±82.5
ATCT	6700±3100	2500±360	330±90	-25±18	-9.5±8.6	-3.7±78.8
CT	3300±1600	1300±180	170±40	-15±15	-5.9±8.3	-4.6±107.6
ATCT_15	8200±1900	2500±350	320±130	-27±17	-8.2±8.2	-3.3±79.5
ATCT_NRT	6000±2200	1900±600	240±120	-21±15	-6.8±7.6	-3.5±78.1

142

8 Figures

Figure 1: Vertical profiles of per component forecast impact of UV, ATCT, and CT experiments

Vertical profiles for the southern hemisphere extra-tropics (left; a,d,g), the tropics (middle; b,e,h), and the northern hemisphere extra-tropics (right; c,f,i), are shown for sampling (top; a,b,c), observation minus 6-hour forecast (middle; d,e,f), and forecast impact (bottom; g,h,i) for the u and v components of MISR CMV in the UV experiment (labeled $uv\ u$ and $uv\ v$ in legend); the along-track ($ATCT\ at$) and cross-track ($ATCT\ ct$) in ATCT; and the cross-track components ($ct\ ct$) in CT.



9

Figure 2: Forecast impact of various observation types in ATCT and ATCT_15 experiments

The mean 24-hour forecast global (top; a,b) and a select regional (bottom; c,d) impact for selected types of observations in the ATCT_15 experiments as accumulated per 6-hours (left; a,c) and per observation (right; b,d). Error bars representing standard deviations are given, alongside percentages of total impact.

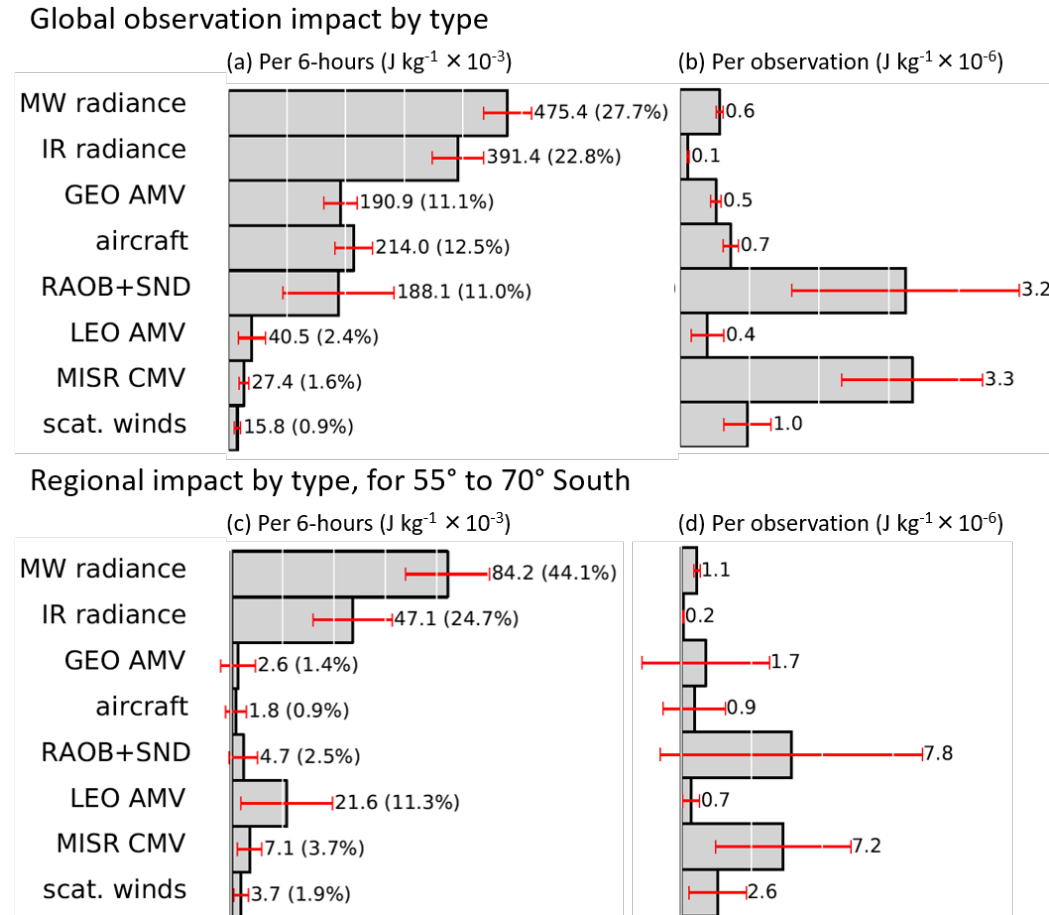
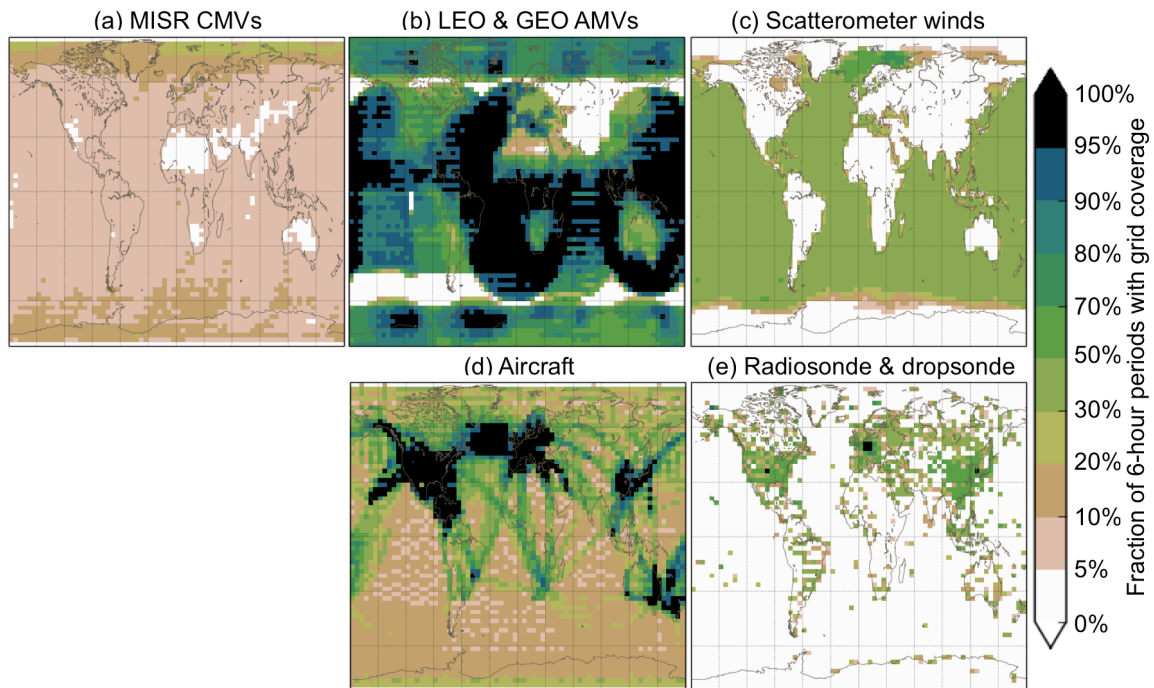


Figure 3: Mapped coverage of MISR CMVs relative to other classes of observation

Mapped coverage for five classes of observations assimilated in ATCT and ATCT_15 experiments spanning Sep.-Nov. 2014 and Mar.-May 2015. Coverage is measured per 2.5° latitude \times 2.5° longitude map grid cell by the fraction of six-hour periods throughout experiments during which one or more observations were assimilated within that grid cell.

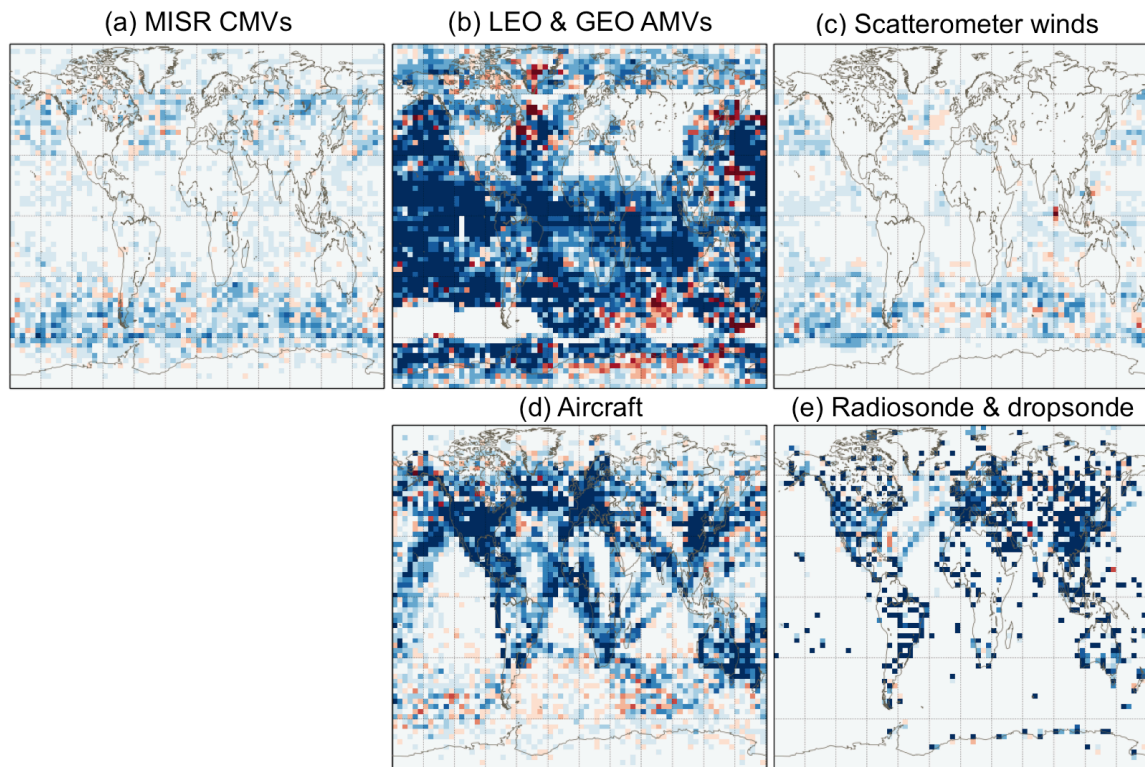


24
25

26 **Figure 4: Adjoint forecast impact of MISR CMVs relative to other classes of observation.**

27 As in Figure 2, but showing mean forecast impact accumulated per six-hour period
28 in each map grid cell.

29



30
31

Figure 5: Time series of MISR CMV sampling and forecast impact per orbit for ATCT and ATCT_15

Time series of forecast impacts (top; a,b) and observation counts (bottom; c,d) for MISR CMV data during ATCT experiment (left; a,c) from Sep.-Nov. 2014 and ATCT_15 experiment (right; b,d) from Mar.-May 2015. Orbits with a net negative (i.e. beneficial) forecast impact are indicated in blue, the rest in red. Minima and maxima are shown in upper right. A running mean over 15 orbits (i.e. ~ 1 day) is plotted in black. Numbers of observations per orbit that were assimilated (blue) and rejected (red) are shown alongside a 15 orbit running mean (black).

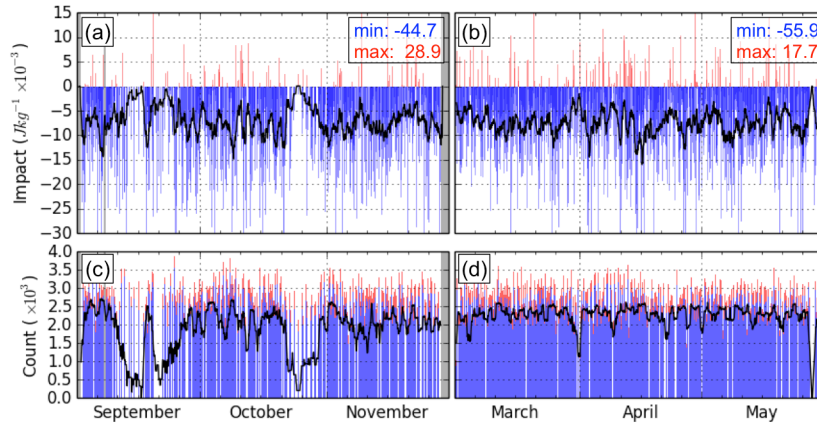


Figure 6: Time series of MISR CMV sampling and forecast impact per orbit for NRT

As in Figure 5, but for experiment NRT.

